

NavFormer: IGRF Forecasting in Moving Coordinate Frames

Yontae Hwang^{1 2 3} Dongwoo Lee⁴ Minseok Choi^{2 3 4} Yong Sup Ihn⁵ Daham Kim^{2 3 *} Deok-Young Lee^{2 3 4 *}

Triad magnetometer components change with sensor attitude even when the IGRF total intensity target stays invariant. NavFormer forecasts this invariant target with rotation invariant scalar features and a Canonical SPD module that stabilizes the spectrum of window level second moments of the triads without sign discontinuities. The module builds a canonical frame from a Gram matrix per window and applies state dependent spectral scaling in the original coordinates. Experiments across five flights show lower error than strong baselines in standard training, few shot training, and zero shot transfer. The code is available at: <https://anonymous.4open.science/r/NavFormer-Robust-IGRF-Forecasting-for-Autonomous-Navigators-0765>

1. Introduction

Moving coordinate frames turn simple forecasting problems into geometry problems. Sensors on drones, aircraft, and wearables record vectors in a body coordinate system. The platform attitude changes over time. The coordinate axes rotate with the sensor. A fixed physical field then produces different channel readings even when the underlying state is unchanged. The IGRF total intensity is such a scalar (Alken et al., 2021). It is invariant to any rotation of the sensor frame. The input includes vector magnetometer triads whose components depend strongly on orientation (Gebre-Egziabher et al., 2006). The learning problem must robustly model physical dynamics despite the spectral instability caused by coordinate choice. Also, in a rotating frame, axis aligned channels do not refer to fixed directions. The component at two times can correspond to different physical vectors. This channel drift introduces structural nonstationarity that is not caused by the underlying field. A forecaster then allocates capacity to adapt to varying signal scales instead of learning the field evolution. The effect intensifies when the training set does not cover the test orientation

¹Graduate School of Data Science, Pusan National University, Busan, Republic of Korea ²OAQ Co. Ltd., Republic of Korea ³Arrakis Technologies Corp., USA ⁴Korea Advanced Institute of Science and Technology, Daejeon, Republic of Korea ⁵Agency for Defense Development, Daejeon, Republic of Korea. Correspondence to: Deok-Young Lee <dleao@oaqcorp.com>, Daham Kim <daham.kim@oaqcorp.com>.

Preprint. January 28, 2026.

distribution. Few shot training and zero shot transfer then suffer even when the target is invariant.

Existing approaches often try to remove rotation dependence before sequence modeling. One option uses only rotation invariant scalars such as norms and dot products (Bulling et al., 2014; Canciani & Brennan, 2020). This yields stable inputs but it discards directional information that encodes vector interactions and dynamics. Another option canonicalizes vectors by projecting them into a data derived basis such as a PCA eigenframe (Jolliffe, 2011; Li et al., 2021). Canonicalization can standardize orientation but eigenvectors are defined only up to an independent sign. Small perturbations can flip an eigenvector sign and create a discontinuous representation (Davis & Kahan, 1970). Discontinuities break the smooth dependence that gradient based optimization assumes (Ionescu et al., 2015). Geometric deep learning instead encodes group structure through equivariant and steerable architectures (Cohen & Welling, 2016; Fuchs et al., 2020; Satorras et al., 2021). These methods show that inductive bias for symmetry can improve data efficiency. Our setting still requires a continuous representation that preserves raw vector dynamics for forecasting.

This paper follows a different principle. We do not need strict invariance at the input. We use a window level conditioning step that stabilizes the scale and condition number of the triad second moment. We compute a Gram matrix within each window and apply spectral reweighting in its principal directions. A symmetric positive definite transform provides a continuous geometric preconditioning (Huang & Van Gool, 2017). The transform reduces anisotropy of the uncentered second moment and ensures a numerically well-conditioned optimization landscape. This helps the downstream transformer spend less capacity on scale correction. The model still receives directional information and it can exploit cross axis structure.

2. Related Works

2.1. Geometric Constraints in Time Series Forecasting

Transformer forecasters model long range dependencies with attention and tokenization choices (Wen et al., 2022). Patch based and variate based designs such as PatchTST (Nie, 2022) and iTransformer (Liu et al., 2023) improve

efficiency and cross channel reasoning, and Crossformer (Zhang & Yan, 2023) further structures attention over channel and temporal axes. Linear baselines such as DLinear (Zeng et al., 2023) show that simple temporal heads can be competitive when channel semantics are stable. These models usually treat each channel as a fixed semantic entity across windows (Chen et al.). Rotating sensing breaks that assumption. For triad measurements, an unknown attitude rotation mixes the three components, so the meaning of each channel shifts while the prediction target can remain approximately rotation invariant (Crassidis et al., 2005). A standard forecaster must learn an implicit coordinate transformation before it can learn temporal dynamics. This makes coordinate system transformation a bottleneck, and it becomes worse under limited training coverage of orientations.

Geometric deep learning builds equivariance into the architecture through group actions, including group equivariant convolution (Cohen & Welling, 2016) and equivariant attention and message passing (Fuchs et al., 2020; Satorras et al., 2021). Most of this work targets spatial prediction on sets, graphs, or short horizon dynamics, rather than long horizon forecasting with heterogeneous scalar and vector channels. Magnetic navigation and aeromagnetic compensation historically address rotation and platform effects through calibration models and recursive estimation, often built around Kalman filtering (Kalman, 1960) and physics based compensation models such as Tolles Lawson (Tolles & Lawson, 1950; Leliak, 2009). Modern airborne magnetic anomaly navigation uses these components together with map information and inertial sensing (Canciani & Brennan, 2020). NavFormer targets the same bottleneck but replaces an explicit attitude and compensation stack with a learned forecaster that injects a geometric inductive bias at the representation level.

2.2. Stable Canonicalization via SPD Manifold

A common route to rotation robustness is canonicalization. One computes a window level second moment, extracts an eigenframe, and projects vectors into that frame. This can reduce nuisance rotations, but it can also introduce discontinuities. Eigenvectors have a sign ambiguity, and near degenerate spectra cause axis instability, so small input perturbations can induce discrete flips or basis drift (Davis & Kahan, 1970; Yu et al., 2015). Riemannian learning on the SPD cone provides tools to model second order statistics without leaving the manifold (Arsigny et al., 2007). SPDNet and later normalization layers define architectures that preserve positive definiteness and respect SPD geometry (Huang & Van Gool, 2017; Bronstein et al., 2021). Prior work often treats SPD matrices as the primary feature type for classification or recognition (Tuzel et al., 2006). NavFormer uses SPD structure as a learnable preconditioner for vector time series rather than as an endpoint representation.

It extracts a canonical eigenframe from a triad Gram matrix, then applies a state conditioned SPD transform that performs spectral reweighting in that eigenframe while acting in the original coordinates. This avoids the sign flip discontinuity that appears in explicit projections, since the induced SPD map is invariant to eigenvector sign choices. The result can reduce anisotropy of the window second moment and can make the condition number and axis scale more consistent across windows. This can give the downstream transformer an input space that is easier to optimize for forecasting.

3. NavFormer

We forecast IGRF total intensity from sensor data (Gnadt et al., 2023b;a). The primary challenge involves the variability of the sensor’s coordinate frame throughout the recording. While the underlying magnetic field magnitude is independent of the sensor’s orientation, the raw observations are heavily dependent on it. To address this, we propose an architecture designed with a geometric inductive bias (Cohen & Welling, 2016). We augment the input with analytically rotation-invariant scalars and apply a geometrically regularized vector modulation layer (Fuchs et al., 2020; Satorras et al., 2021). This layer applies SPD based spectral reweighting of the triads in a data driven canonical frame, using the global state summary. Unlike rigid projections that introduce discontinuities our approach aligns the signal statistics while maintaining numerical stability. The resulting spectrally reweighted representation is processed by a grid transformer for sequence modeling.

3.1. Problem Setting

Let $X \in \mathbb{R}^{L \times D_0}$ be an input window of length L with D_0 channels. These input features are heterogeneous. At each time step t , the slice is $x_t = (B_t, C_t, D_t, r_t)$, where $B_t, C_t, D_t \in \mathbb{R}^3$ are the triad vectors and r_t collects scalar telemetry. The IGRF magnitude is our prediction target and remains invariant under changes in the sensor coordinate frame. We model a change in the sensor coordinate frame as a rotation $R \in \mathbf{SO}(3)$. The attitude change is small, Within each input window, we approximate this change as fixed rotation R , which captures piecewise constant orientation over the window. This rotation acts on the triad vectors (B_t, C_t, D_t) while leaving the non triad variables r_t unchanged $(B_t, C_t, D_t, r_t) \mapsto (RB_t, RC_t, RD_t, r_t)$.

Our goal is to forecast an IGRF total intensity $y \in \mathbb{R}^{L_{\text{pred}} \times 1}$ over a horizon L_{pred} given the input X . A naive model must learn to internalize the rotation group structure entirely from data to map the rotating X to the invariant y . Instead of enforcing strict invariance we use a geometrically adaptive conditioning step. The step rescales the triad second moment within each window to reduce anisotropy and stabilize the condition number seen by the sequence model.

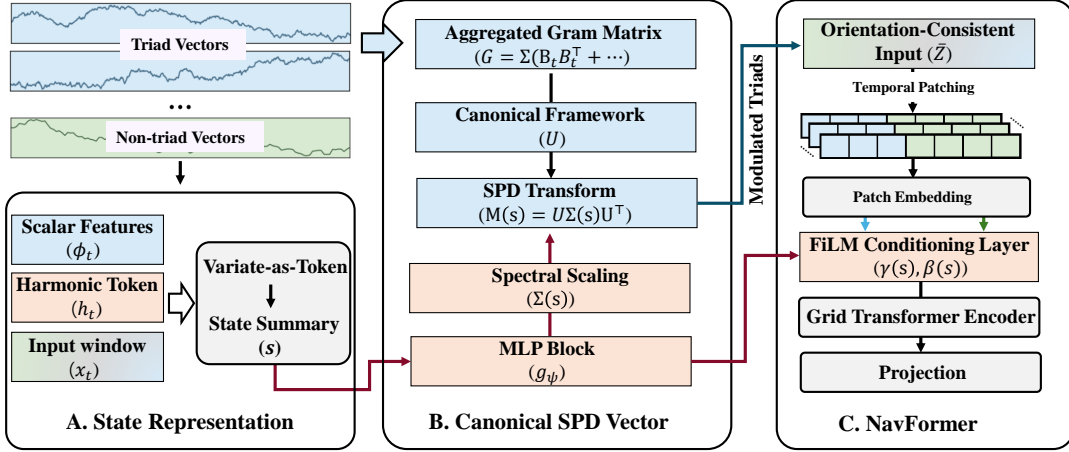


Figure 1. Overview of the NavFormer architecture.

This helps the model learn temporal dynamics in a feature space with more consistent axis scaling, while preserving directional information.

3.2. Scalar Geometric Features

From the vector triads $B_t, C_t, D_t \in \mathbb{R}^3$, we construct scalar features that are naturally insensitive to orientation. For three vectors, we define the per-time-step feature

$$\phi_t := [\mathbf{n}_t^\top, \mathbf{d}_t^\top, \mathbf{c}_t^\top]^\top \in \mathbb{R}^9, \quad (1)$$

Where $\mathbf{n}_t = [\|B_t\|, \|C_t\|, \|D_t\|]^\top$ contains the norms, \mathbf{d}_t contains the pairwise dot products, and \mathbf{c}_t contains the cross product norms. Equation (1) is analytically invariant under joint rotations of (B_t, C_t, D_t) . To capture temporal dynamics, we encode time using a fixed bank of sinusoidal harmonic tokens, motivated by Fourier feature mappings (Tancik et al., 2020). For sampling frequency f_s and predefined frequencies $\{f_k\}_{k=1}^K$, we let $\tau_t := t/f_s$ and define

$$h_t := \left[\sin(2\pi f_k \tau_t), \cos(2\pi f_k \tau_t) \right]_{k=1}^K \in \mathbb{R}^{2K}. \quad (2)$$

The concatenated per-step feature thus reads $u_t := [x_t; \phi_t; h_t] \in \mathbb{R}^{D_0+9+2K}$. We stack $(u_t)_{t=1}^L$ over time yields the augmented sequence

$$Z := [u_1, \dots, u_L]^\top \in \mathbb{R}^{L \times D_{\text{aug}}}, \quad (3)$$

Where $D_{\text{aug}} := D_0 + 9 + 2K$. Next, to capture the global temporal dynamics of each feature while isolating rotation-invariant information, we adopt a variate-as-token strategy (Liu et al., 2023). Therefore, we treat each variable channel as an independent token. Specifically, we transpose the augmented sequence Z and apply a learnable linear projection $W \in \mathbb{R}^{d \times L}$ along the temporal dimension

$$e_c = W(Z_{:,c}) + b \in \mathbb{R}^d, \quad c = 1, \dots, D_{\text{aug}}. \quad (4)$$

This operation compresses the time series of the c -th variable into a single d -dimensional embedding e_c . Building on this representation, we construct a global context vector designed to remain robust against sensor orientation. We divide the feature indices $\{1, \dots, D_{\text{aug}}\}$ into two distinct sets \mathcal{M} and \mathcal{S} . \mathcal{M} holds the raw vector channels subject to rotation. \mathcal{S} contains the rotation-invariant channels, including r_t , ϕ_t , and h_t . We then compute the state summary s by averaging the embeddings of the invariant set

$$s := \frac{1}{|\mathcal{S}|} \sum_{c \in \mathcal{S}} e_c \in \mathbb{R}^d. \quad (5)$$

Because every feature within \mathcal{S} is immune to the rotation action, the resulting summary s provides a comparatively stable, frame-independent anchor. Conditioning the geometric modulation layers on s helps the model adapt its frame-dependent processing using a state signal that remains consistent across sensor orientations.

3.3. Canonical SPD module

We introduce the Canonical SPD module as a geometric preconditioner. While the scalar features ϕ_t provide a rotation-invariant anchor, the vector channels retain directional information essential for physical consistency. It rescales the window aggregated uncentered 2nd moment of the triad vectors. The modulation depends on the global state summary. The output triads transform by the same rotation as the input triads. Functionally, the process is twofold. First, we extract a canonical frame from an aggregated triad Gram matrix. Second, we apply a state dependent spectral reweighting within that frame using an SPD transform (Huang & Van Gool, 2017; Li et al., 2018). A standard approach to geometric learning involves projecting input vectors onto a canonical basis U (e.g., computing $U^\top B_t$) to achieve invariance. However, eigenvectors U are only defined up to a sign flip ($u \leftrightarrow -u$). This sign ambiguity creates discontinuity in the projected features, as small

perturbations in the input can cause discrete jumps in the representation. Such instability hinders the optimization of continuous forecasting models. To resolve this, we employ a spectral modulation $M(\mathbf{s}) = U\Sigma(\mathbf{s})U^\top$. This transform operates in the global frame and is invariant to the sign choice of U , as $(-U)\Sigma(-U)^\top = U\Sigma U^\top$. Therefore this component acts as a geometric preconditioner. It rescales energy along the principal axes of the aggregated uncentered second moment. This removes the sign flip ambiguity of eigenvectors. This can reduce anisotropy in the second moment.

Canonical Frame from Aggregated Gram Matrix To establish a stable geometric reference, we compute an aggregated Gram matrix for a window of triad vectors $\{B_t, C_t, D_t\}_{t=1}^L$. This matrix is an uncentered 2nd moment statistic of the triad vectors over the window.

$$G := \sum_{t=1}^L (B_t B_t^\top + C_t C_t^\top + D_t D_t^\top) \in \mathbb{R}^{3 \times 3}. \quad (6)$$

By definition, G is symmetric and positive semi-definite. We perform an eigen-decomposition $G = U\Lambda U^\top$, yielding eigenvalues $\lambda_1 \geq \lambda_2 \geq \lambda_3 \geq 0$ and orthonormal eigenvectors $U = [u_1 u_2 u_3] \in \mathbb{R}^{3 \times 3}$. We designate U as the canonical frame, as it intrinsically maps the window's dominant directions of variation. To ensure that the canonical frame is numerically stable, we use a mild separation assumption on the aggregated Gram matrix G . Specifically, for the vast majority of windows, we assume G has three distinct eigenvalues with a non-trivial spectral gap: there exists $\delta > 0$ such that

$$\frac{\lambda_1 - \lambda_2}{\lambda_1 + \epsilon} \geq \delta, \quad \frac{\lambda_2 - \lambda_3}{\lambda_2 + \epsilon} \geq \delta. \quad (7)$$

Under this assumption, the eigenbasis U is unique up to independent sign flips and varies smoothly with G , which is crucial for continuity of the canonicalization map.

State-Dependent SPD Scaling We map the state summary $\mathbf{s} \in \mathbb{R}^d$ (defined in Section 3.2) to three scalar scales via an MLP

$$\mathbf{d}(\mathbf{s}) = (d_1, d_2, d_3) = g_\psi(\mathbf{s}) \in \mathbb{R}^3, \quad (8)$$

where g_ψ is a lightweight neural network. Each scalar d_i targets one of the three canonical eigenvectors (u_1, u_2, u_3) derived from the aggregated Gram matrix, allowing the model to independently modulate signal energy along each principal axis. To reduce excessive contraction along any canonical axis, we impose a lower bound of ϵ on the scales

$$\sigma_i(\mathbf{s}) := \epsilon + \text{softplus}(d_i), \quad i = 1, 2, 3. \quad (9)$$

These scales form a diagonal matrix

$$\Sigma(\mathbf{s}) := \text{diag}(\sigma_1(\mathbf{s}), \sigma_2(\mathbf{s}), \sigma_3(\mathbf{s})) \in \mathbb{R}^{3 \times 3}. \quad (10)$$

We use it as a safeguard against near zero scaling that would suppress a direction of the triad signal. The model can still adjust the relative weighting across canonical directions through $\Sigma(\mathbf{s})$. We then define the resulting canonical SPD transform as

$$M(\mathbf{s}) := U\Sigma(\mathbf{s})U^\top \in \text{SPD}(3), \quad (11)$$

where $\text{SPD}(3)$ is the cone of 3×3 symmetric positive definite matrices. Applying $M(\mathbf{s})$ to the input triads yields the modulated sequences

$$\tilde{B}_t := M(\mathbf{s})B_t, \quad \tilde{C}_t := M(\mathbf{s})C_t, \quad \tilde{D}_t := M(\mathbf{s})D_t. \quad (12)$$

The following proposition confirms that $M(\mathbf{s})$ preserves the canonical eigenvectors while selectively reweighting the covariance spectrum.

Proposition 3.1 (Spectral Alignment of Canonical SPD). *Let $G = U\Lambda U^\top$ be the aggregated Gram matrix and $M(\mathbf{s}) = U\Sigma(\mathbf{s})U^\top$ the canonical SPD transform. Define the Gram matrix of the modulated triads as*

$$\tilde{G}(\mathbf{s}) := \sum_{t=1}^L (\tilde{B}_t \tilde{B}_t^\top + \tilde{C}_t \tilde{C}_t^\top + \tilde{D}_t \tilde{D}_t^\top). \quad (13)$$

Then

$$\tilde{G}(\mathbf{s}) = U\Sigma(\mathbf{s})\Lambda\Sigma(\mathbf{s})U^\top. \quad (14)$$

In particular, $\tilde{G}(\mathbf{s})$ has eigenvectors U and eigenvalues $\sigma_i(\mathbf{s})^2 \lambda_i$ for $i = 1, 2, 3$.

Proof. See Appendix B. □

Proposition 3.1 demonstrates that the Canonical SPD reweights the spectrum of the triad Gram matrix. While the output vectors \tilde{B}_t remain rotation-equivariant, their statistical structure is stabilized. This spectral normalization acts as a geometric preconditioner, providing the downstream forecaster with a numerically well-conditioned input space that is easier to optimize. Their window aggregated uncentered 2nd moment becomes $\tilde{G}(\mathbf{s}) = U\Sigma(\mathbf{s})\Lambda\Sigma(\mathbf{s})U^\top$. This can reduce variation in the spectrum of the second moment across windows. The downstream sequence model then receives inputs with a more consistent spectrum. This can improve numerical conditioning during training.

3.4. Patch-Channel Grid Transformer

The Canonical SPD module and invariant scalar augmentation yield a sequence that is geometrically regularized, serving as the input to our patch-channel grid transformer. We define the feature slice $\bar{x}_t \in \mathbb{R}^{D_0}$ by substituting the raw magnetometer triads with their SPD-modulated counterparts $(\tilde{B}_t, \tilde{C}_t, \tilde{D}_t)$. All other channels, including scalar telemetry,

are preserved in their original form. The invariant scalars ϕ are derived from the raw triads (B_t, C_t, D_t) before any SPD modulation occurs to preserve the original signal intensity information. We assemble the final spectrally reweighted vector for each step as

$$\bar{u}_t := [\bar{x}_t; \phi_t; h_t] \in \mathbb{R}^{D_{\text{aug}}}. \quad (15)$$

where $D_{\text{aug}} = D_0 + 9 + 2K$. These are stacked temporally to form the input tensor as here:

$$\bar{Z} := [\bar{u}_1, \dots, \bar{u}_L]^\top \in \mathbb{R}^{L \times D_{\text{aug}}}. \quad (16)$$

To efficiently resolve both temporal dependencies and cross-channel interactions (Zhang & Yan, 2023) within \bar{Z} , we utilize a grid based self-attention mechanism operating on channel-specific patches.

Temporal Patching per Channel We process each channel independently by extracting overlapping temporal patches (Nie, 2022). Let P denote the patch length and S the stride. To guarantee full coverage at the sequence boundaries, we apply replication padding of S time steps to the end of the sequence, resulting in an effective length of $L + S$. The number of patches is then $M_p := \lfloor \frac{L-P}{S} \rfloor + 2$.

Working from a channel-first perspective $\bar{Z}^\top \in \mathbb{R}^{D_{\text{aug}} \times L}$, we define the temporal patch vector for channel $c \in \{1, \dots, D_{\text{aug}}\}$ and patch index $m \in \{1, \dots, M_p\}$

$$z_{c,m} := [\bar{Z}_{c,(m-1)S+1}^\top, \dots, \bar{Z}_{c,(m-1)S+P}^\top]^\top \in \mathbb{R}^P, \quad (17)$$

where any indices exceeding the original length L are populated via the replication padding.

Patch Embedding We map each raw patch into the model dimension d via a shared linear projection as here

$$p_{c,m} := W_{\text{patch}} z_{c,m} + b_{\text{patch}} \in \mathbb{R}^d, \quad (18)$$

with weights $W_{\text{patch}} \in \mathbb{R}^{d \times P}$ and bias $b_{\text{patch}} \in \mathbb{R}^d$. This operation yields a structured 2D grid of tokens $\{p_{c,m}\}$, indexed by channel c and patch m . These embeddings encode local temporal patterns, forming the substrate for the global state-conditioning mechanism described next.

FiLM Conditioning of Token Embeddings To ground the local embeddings in the global system state, we modulate the patch tokens $p_{c,m}$ using the summary vector $s \in \mathbb{R}^d$ (derived in Sec. 3.2). We compute the affine FiLM parameters via a projection network q_ω as

$$\begin{aligned} (\hat{\gamma}(s), \beta(s)) &= q_\omega(s) \in \mathbb{R}^{2d}, \\ \gamma(s) &:= 1 + \tanh(\hat{\gamma}(s)). \end{aligned} \quad (19)$$

This modulation is applied selectively. We apply it only to the magnetometer channels so vector token processing

depends on the global state summary. We set $\tilde{p}_{c,m} := \gamma(s) \odot p_{c,m} + \beta(s)$ with $c \in \mathcal{M}$. Auxiliary telemetry channels remain unchanged, so $\tilde{p}_{c,m} := p_{c,m}$ with $c \notin \mathcal{M}$. This mechanism diffuses global state context across the token grid. The tanh bounded scaling factor $\gamma(s)$ helps keep the modulation stable. Finally, we add learnable embeddings for channel index and patch index, then flatten the grid into a unified token sequence of length $D_{\text{aug}} M_p$

$$T := \text{vec}(\{\tilde{p}_{c,m}\}_{c=1, m=1}^{D_{\text{aug}}, M_p}) \in \mathbb{R}^{(D_{\text{aug}} M_p) \times d}, \quad (20)$$

This structure enables the transformer encoder to jointly resolve dependencies across both temporal patches and distinct sensor channels.

Grid Self-Attention Encoder We apply a Transformer encoder (Vaswani et al., 2017) to the flattened token sequence

$$H := \text{Encoder}(T) \in \mathbb{R}^{(D_{\text{aug}} M_p) \times d}. \quad (21)$$

Mapping the output back to the original grid structure recovers a representation $H_{c,m} \in \mathbb{R}^d$ specific to each channel and patch. Since our self-attention spans the full grid, every token effectively possesses a global receptive field. This allows the model to aggregate context from any channel and any temporal patch simultaneously. The result is a architecture that captures rich cross-sensor interactions and long-range temporal reasoning, all while maintaining computational efficiency by operating on a reduced temporal resolution ($M_p \ll L$).

3.5. Channel-Shared Horizon Projection

We adopt a channel shared decoding strategy to synthesize the forecast from the grid representation. The encoder output H preserves the distinct identity of each variable while encoding their temporal dependencies. To generate the prediction we first flatten the patch dimension for each channel independently. This operation collapses the local temporal tokens into a unified channel vector

$$v_c = \text{vec}([H_{c,1}, \dots, H_{c,M_p}]) \in \mathbb{R}^{M_p d} \quad (22)$$

where c indexes both the raw sensor inputs and the geometric invariants. We then apply a linear projection $W_{\text{head}} \in \mathbb{R}^{L_{\text{pred}} \times (M_p d)}$ to map these latent temporal features directly to the forecasting horizon

$$\hat{y}_c = W_{\text{head}} v_c + b_{\text{head}} \in \mathbb{R}^{L_{\text{pred}} \times 1} \quad (23)$$

Crucially we share W_{head} and b_{head} across all D_{aug} channels. This design leverages the variate based tokenization philosophy where the model learns universal temporal dynamics applicable to both magnetic field components and scalar telemetry. It acts as a regularization mechanism that prevents overfitting to channel specific noise.

Panel A. Lookback window $L = 30$ (Avg. over prediction lengths $L_{\text{pred}} \in \{60, 120\}$)																
Methods	NavFormer		PatchTST		PAttn		TimeFilter		iTransformer		TimesNet		DLinear		LTC-CFC	
Metric	MAE	RMSE	MAE	RMSE	MAE	RMSE	MAE	RMSE	MAE	RMSE	MAE	RMSE	MAE	RMSE	MAE	RMSE
NV2	0.0210	0.0595	0.0226	0.0632	0.0225	0.0636	0.0225	0.0657	0.0237	0.0661	0.0287	0.0747	0.0737	0.1194	0.2883	0.3769
NV3	0.0351	0.0802	0.0349	0.0792	0.0369	0.0816	0.0403	0.0965	0.0380	0.0826	0.0486	0.0944	0.1125	0.1637	0.2321	0.2974
NV4	0.0238	0.0774	0.0261	0.0798	0.0354	0.0908	0.0439	0.1076	0.0516	0.1060	0.0607	0.1214	0.1299	0.1825	0.3507	0.4428
NV6	0.1216	0.2683	0.1336	0.2737	0.1480	0.2950	0.1488	0.2970	0.1592	0.3061	0.1913	0.3492	0.3145	0.4871	0.3591	0.4387
NV7	0.0520	0.1005	0.0532	0.1040	0.0575	0.1070	0.0607	0.1181	0.0670	0.1135	0.0567	0.1025	0.1238	0.1727	0.3526	0.4256
Avg. Rank	1.3	1.4	2.2	2.0	3.1	3.0	3.9	3.9	4.5	3.9	6.0	6.0	7.0	7.0	8.0	8.0

Panel B. Lookback window $L = 60$ (Avg. over prediction lengths $L_{\text{pred}} \in \{60, 120\}$)																
Methods	NavFormer		PatchTST		PAttn		TimeFilter		iTransformer		TimesNet		DLinear		LTC-CFC	
Metric	MAE	RMSE	MAE	RMSE	MAE	RMSE	MAE	RMSE	MAE	RMSE	MAE	RMSE	MAE	RMSE	MAE	RMSE
NV2	0.0215	0.0637	0.0252	0.0658	0.0228	0.0647	0.0239	0.0683	0.0233	0.0681	0.0315	0.0773	0.2281	0.1025	0.2848	0.3783
NV3	0.0404	0.0916	0.0408	0.0869	0.0409	0.0916	0.0442	0.0996	0.0412	0.0894	0.0522	0.1021	0.1044	0.1544	0.2231	0.2905
NV4	0.0251	0.0836	0.0287	0.0804	0.0327	0.0881	0.0307	0.0891	0.0462	0.1015	0.0586	0.1226	0.1144	0.1668	0.3528	0.4446
NV6	0.1365	0.2889	0.1366	0.2807	0.1398	0.2948	0.1450	0.2961	0.1602	0.3130	0.2036	0.3753	0.3551	0.5404	0.3591	0.4383
NV7	0.0578	0.1112	0.0574	0.1121	0.0633	0.1190	0.0611	0.1166	0.0611	0.1098	0.0782	0.1333	0.1047	0.1537	0.3565	0.4323
Avg. Rank	1.5	2.5	2.7	1.9	3.4	2.8	4.6	4.2	3.8	3.7	5.8	5.9	7.0	7.0	8.0	8.0

Table 1. Forecasting performance comparison on the IGRF dataset. We report the Mean Absolute Error (MAE) and Root Mean Squared Error (RMSE) averaged over prediction lengths $T \in \{60, 120\}$. **Panel A** presents results with a lookback window of $L = 30$, while **Panel B** uses a lookback window of $L = 60$. The best results are highlighted in red, the second-best in blue and third-best in bold, respectively. Full results for each specific prediction length are provided in the Appendix D.

4. Experiment

We evaluate the proposed NavFormer on the task of forecasting the IGRF total intensity from rotating vector magnetometer data. We compare the method against state of the art time series forecasting models. We analyze performance in standard, few shot, and zero shot settings. We also analyze the contribution of the geometric components through ablation and spectral stability checks.

4.1. Implementation details

Dataset The magnetometer dataset(Gnadt et al., 2020) contains multiple flights of a fixed wing aircraft. The platform carries several vector fluxgate sensors and scalar magnetometers that record the local geomagnetic field together with auxiliary telemetry. Scalar magnetometer is mounted at the end of the tail stinger and serves as a reference IGRF total intensity. Flights NV2, NV3, NV4, NV6, and NV7 cover compensation maneuvers, free flight segments, and regional survey lines over Eastern Ontario and nearby regions. The raw recordings form multivariate time series of vector triads and scalar channels with long temporal context. For each flight we split the time axis into contiguous train, validation, and test blocks with a 60%, 20%, and 20%, then form windows within each block. Details of the dataset description provided in Appendix A.

Baseline Models We compare NavFormer with patch based and attention based forecasters that represent strong modern sequence modeling baselines. We include PatchTST (Nie, 2022), iTransformer (Liu et al., 2023), and PAttn (Tan et al., 2024). We also include TimesNet (Wu et al., 2022) and the linear model DLinear (Zeng et al., 2023). We report results for two additional baselines, TimeFilter (Hu et al., 2025) and LTC-CFC (Nerrise et al., 2024). For each baseline, we tune hyperparameters on the validation split and

select the checkpoint with the lowest validation error before reporting test performance. Details of the parameter search space are provided in Appendix C.

Task and metrics Models take an input window of length $L \in \{30, 60\}$ and forecast the IGRF total intensity over horizons $L_{\text{pred}} \in \{60, 120\}$. We report mean absolute error and root mean squared error. We average results over the two horizons in the main tables.

4.2. Main forecasting performance

Results Table 1 compares NavFormer with baselines under two context lengths. With $L = 30$, NavFormer attains the lowest MAE on four out of five flights and the lowest RMSE on four out of five flights. The MAE gains over the strongest baseline reach 8.8% on NV4 and 9.0% on NV6, relative to PatchTST. NV4 and NV6 include stronger attitude variation, which induces pronounced channel drift when triads are expressed in a rotating sensor frame. NavFormer reduces this drift by using a Gram defined canonical frame and a state conditioned SPD spectral scaling that stabilizes triad statistics across orientations. With $L = 60$, NavFormer again achieves the lowest MAE on four out of five flights. The benefit strengthens on NV4 where NavFormer improves MAE by 12.5% relative to PatchTST. These results match the method design. The invariant scalar pathway provides a stable summary of the physical state, while the canonical SPD modulation and FiLM conditioning correct frame dependent variation in the triads and patch tokens. In contrast, baselines process raw triad components as fixed channels. They must infer rotation robustness from data, which requires coverage over sensor orientations and can waste model capacity on coordinate alignment. The poor performance of DLinear and LTC-CFC in Table 1 is consistent with this failure mode, since these models have limited

ability to model nonlinear interactions among rotating vector channels.

4.3. Generalization under limited or shifted supervision

Setting We evaluate generalization under two protocols. In the few shot setting, we train each model on only 5% of the training windows from the target flight while keeping the same validation and test splits. In the zero shot transfer setting, we train on one source flight and evaluate on the remaining flights without fine tuning.

4.3.1. FEW SHOT FORECASTING

Results Table 2 reports performance when training data is limited. NavFormer attains the lowest MAE on every flight and under both lookback lengths. With $L = 30$, NavFormer reduces the average MAE from 0.0996 for PatchTST to 0.0843, which corresponds to a 15.38% reduction. With $L = 60$, the reduction increases from 0.0987 to 0.0809, which corresponds to 18.05%. The largest gap occurs on NV4. For $L = 60$, NavFormer attains MAE 0.0484, while PatchTST attains 0.0805, which corresponds to a 39.88% reduction. These results suggest improved sample efficiency. The rotation invariant scalars provide supervision signals that remain stable across sensor frames. The canonical SPD modulation then maps the vector triads to a representation that varies less with orientation. Baselines must learn this normalization from limited examples, which increases error when the training subset does not cover the orientation distribution of the test windows.

Panel A. Lookback window $L = 30$ (Avg. over prediction lengths $L_{\text{pred}} \in \{60, 120\}$)					
Methods	NavFormer	PatchTST	PAtn	TimeFilter	iTransformer
NV2	0.0326	0.0381	0.0379	0.0341	0.0369
NV3	0.0500	0.0554	0.0625	0.0648	0.0653
NV4	0.0604	0.0782	0.0833	0.0809	0.0852
NV6	0.2061	0.2472	0.2624	0.2411	0.2638
NV7	0.0724	0.0792	0.0858	0.0847	0.0872

Panel B. Lookback window $L = 60$ (Avg. over prediction lengths $L_{\text{pred}} \in \{60, 120\}$)					
Methods	NavFormer	PatchTST	PAtn	TimeFilter	iTransformer
NV2	0.0282	0.0396	0.0380	0.0362	0.0415
NV3	0.0506	0.0566	0.0638	0.0711	0.0745
NV4	0.0484	0.0805	0.0877	0.0916	0.1001
NV6	0.1991	0.2353	0.2477	0.2435	0.3062
NV7	0.0782	0.0816	0.0852	0.0920	0.1016

Table 2. Few shot forecasting. We train each model with a 5% subset of the training windows of the target flight and we keep the same validation and test splits. The best, second-best, and third-best results for each metric are highlighted in red, blue, and bold, respectively.

4.3.2. ZERO SHOT TRANSFER

Results Table 3 measures generalization across flights whose maneuver profiles and orientation statistics differ. NavFormer attains the lowest MAE in nine of ten settings and it achieves the best average MAE in both panels. With $L = 30$, the average MAE decreases from 0.0553 for PatchTST to 0.0530, which corresponds to a 4.16% reduction. With $L = 60$, the average MAE decreases from 0.0603

for PAtn to 0.0587, which corresponds to a 2.65% reduction. The exceptions occur on NV4 with $L = 30$ and on NV6 with $L = 60$, where a baseline attains slightly lower MAE. The advantage persists under this stronger distribution shift because NavFormer encodes the symmetry of the task. The state summary depends on channels that are invariant to $\text{SO}(3)$ rotations, so the conditioning signals remain comparable across flights. The canonical frame derives from the Gram matrix of the triads within each window, so it adapts to orientation changes without requiring flight specific training.

Panel A. Lookback window $L = 30$ (Avg. over prediction lengths $L_{\text{pred}} \in \{60, 120\}$)					
Methods	NavFormer	PatchTST	PAtn	TimeFilter	iTransformer
NV2	0.0608	0.0690	0.0638	0.0673	0.0692
NV3	0.0511	0.0540	0.0541	0.0559	0.0599
NV4	0.0596	0.0587	0.0651	0.0720	0.0794
NV6	0.0396	0.0403	0.0399	0.0421	0.0439
NV7	0.0537	0.0543	0.0569	0.0597	0.0636

Panel B. Lookback window $L = 60$ (Avg. over prediction lengths $L_{\text{pred}} \in \{60, 120\}$)					
Methods	NavFormer	PatchTST	PAtn	TimeFilter	iTransformer
NV2	0.0647	0.0795	0.0676	0.0745	0.0696
NV3	0.0597	0.0626	0.0629	0.0635	0.0619
NV4	0.0667	0.0751	0.0705	0.0713	0.0786
NV6	0.0434	0.0485	0.0409	0.0412	0.0445
NV7	0.0588	0.0677	0.0596	0.0593	0.0658

Table 3. Zero shot forecasting. We train on source flights and evaluate on the held out flight without parameter updates. The best, second-best, and third-best results for each metric are highlighted in red, blue, and bold, respectively.

4.4. Mechanism analysis

Ablation Studies We ablate four components of NavFormer under both input lengths. Table 4 reports the relative MAE increase for each ablation, defined as

$$\Delta\% = 100 \times (\text{MAE}_{\text{abl}} - \text{MAE}_{\text{full}}) / \text{MAE}_{\text{full}}. \quad (24)$$

Removing harmonic tokens increases MAE on every flight. With $L = 30$, the increase ranges from 3.81 to 5.85% with a mean of 5.05%. With $L = 60$, the mean increase is 3.14%. This supports that explicit temporal harmonics compensate for limited context. Removing the canonical SPD modulation also degrades performance. With $L = 30$, the mean increase is 4.03% and the increase reaches 6.21% on NV6. With $L = 60$, the mean increase is 2.67%, but NV7 still shows a 5.88% increase. This supports that geometry aware modulation matters most when orientation variability is high.

Removing FiLM has a smaller effect for $L = 30$, with a mean increase of 2.56%, but it has the largest effect for $L = 60$, with a mean increase of 4.37%. The increase reaches 10.85% on NV7. Longer context improves the state summary and strengthens the effect of state conditioned token modulation. The Only FiLM variant, which keeps FiLM while removing harmonic tokens and canonical SPD modulation, also underperforms the full model. Its mean increase is 2.94% for $L = 30$ and 4.35% for $L = 60$. These results show that FiLM alone cannot replace the combination of temporal priors and canonical SPD modulation.

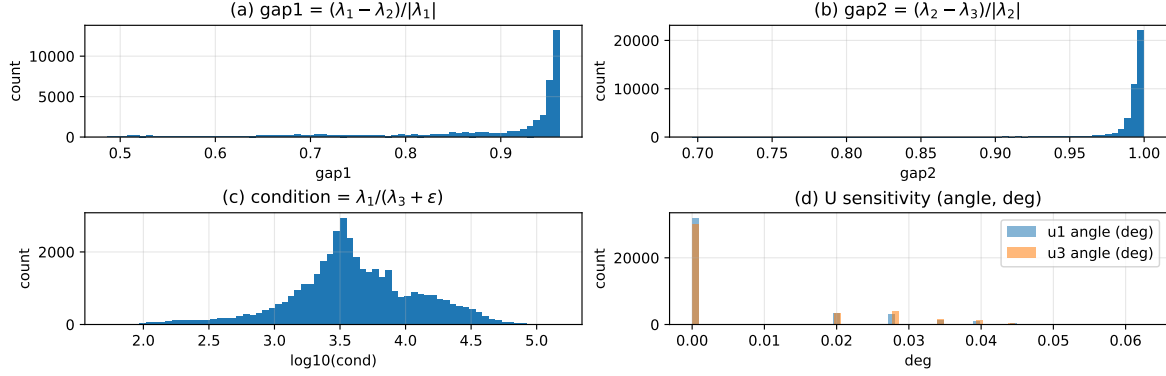


Figure 2. Spectrum and stability statistics of the aggregated Gram matrix G over test windows.

Methods	Relative Performance Drop (%) ↓			
	w/o Harmonic	w/o SPD	w/o FiLM	Only FiLM
Panel A. Sequence Length $L = 30$				
NV2	4.85	3.14	2.20	2.15
NV3	3.81	5.15	0.46	3.89
NV4	5.85	1.83	2.54	1.75
NV6	4.97	6.21	6.62	2.77
NV7	5.76	3.82	0.99	4.13
Panel B. Sequence Length $L = 60$				
NV2	2.97	0.72	1.65	2.38
NV3	3.96	0.43	1.25	3.27
NV4	2.72	3.55	3.27	3.67
NV6	2.67	2.75	4.81	5.87
NV7	3.40	5.88	10.85	6.55

Table 4. Ablation study for NavFormer. Panel A uses input length $L = 30$ and Panel B uses input length $L = 60$. We report the relative MAE increase in % with respect to the full model.

Stability of the canonical frame We examine when the eigenframe of the aggregated Gram matrix G is identifiable and stable over the test distribution. For each input window we compute eigenvalues $\lambda_1 \geq \lambda_2 \geq \lambda_3$ and the relative gaps 6. We also compute the condition proxy $\kappa = \lambda_1/(\lambda_3 + \epsilon)$ for a small ϵ . To test stability, we add a small perturbation to the triads, recompute the eigenvectors, and measure the angle between each original eigenvector u_i and its perturbed counterpart \tilde{u}_i . Figure 2 shows that both gap statistics concentrate near 1. This implies strong spectral separation in most windows, which makes the canonical basis close to unique up to sign (Davis & Kahan, 1970; Yu et al., 2015). The distribution of $\log_{10} \kappa$ is broad and often large, which indicates anisotropic energy across canonical directions and supports direction wise SPD scaling.

The eigenvector perturbation angles for u_1 and u_3 concentrate near 0° and remain below about 0.06° on almost all windows. This stability implies that small sensor noise does not materially change the canonical axes, so the learned SPD scaling admits a consistent interpretation as axis aligned gain control. A small subset of windows sits in the lower tail of the gap distribution. In those cases the eigenframe can drift within a nearly degenerate subspace. NavFormer retains a stable conditioning signal through the invariant scalar pathway, which does not depend on the eigenframe.

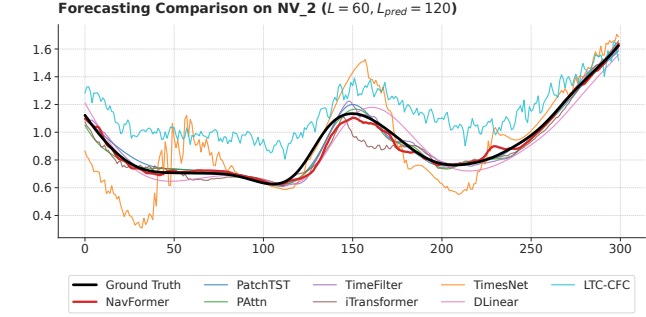


Figure 3. Forecasting comparison on NV2 with lookback $L = 60$ and prediction horizon $L_{\text{pred}} = 120$.

Show Case Analysis We visualize a representative forecast on NV2 with lookback $L = 60$ and horizon $L_{\text{pred}} = 120$ in Figure 3. NavFormer follows the ground truth trajectory through the steep rise near $t \approx 130$ and the subsequent decline, and it preserves the amplitude during the final increase. PatchTST and PAtn capture the global trend but smooth the peak and show a small lag around turning points. iTransformer and DLinear underestimate the mid horizon peak and the late horizon rise. TimesNet produces oscillatory deviations and overshoots, while LTC-CFC exhibits a sustained positive bias over much of the segment. This example aligns with Table 1 and supports the role of the geometric front end in reducing frame-dependent variation.

5. Conclusion

NavFormer targets forecasting with rotating vector sensors by aligning window statistics instead of enforcing strict input invariance. The model combines rotation invariant scalar features with a sign invariant canonical symmetric positive definite spectral transform of triad vectors. Experiments on five aircraft flights show the best mean absolute error on most flights and consistent gains over strong transformer baselines. Few shot and zero shot tests show that the geometric front end improves sample efficiency and cross flight transfer. More broadly, the proposed framework is compatible with sensing pipelines (Lee et al., 2026; 2024).

References

- Alken, P., Thébault, E., Beggan, C. D., Amit, H., Aubert, J., Baerenzung, J., Bondar, T., Brown, W., Califf, S., Chambodut, A., et al. International geomagnetic reference field: The thirteenth generation. *Earth, Planets and Space*, 73(1):49, 2021.
- Arsigny, V., Fillard, P., Pennec, X., and Ayache, N. Geometric means in a novel vector space structure on symmetric positive-definite matrices. *SIAM journal on matrix analysis and applications*, 29(1):328–347, 2007.
- Bronstein, M. M., Bruna, J., Cohen, T., and Veličković, P. Geometric deep learning: Grids, groups, graphs, geodesics, and gauges. *arXiv preprint arXiv:2104.13478*, 2021.
- Bulling, A., Blanke, U., and Schiele, B. A tutorial on human activity recognition using body-worn inertial sensors. *ACM Computing Surveys (CSUR)*, 46(3):1–33, 2014.
- Canciani, A. J. and Brennan, C. J. An analysis of the benefits and difficulties of aerial magnetic vector navigation. *IEEE Transactions on Aerospace and Electronic Systems*, 56(6):4161–4176, 2020.
- Chen, Y., Céspedes, N., and Barnaghi, P. A closer look at transformers for time series forecasting: Understanding why they work and where they struggle. In *Forty-second International Conference on Machine Learning*.
- Cohen, T. and Welling, M. Group equivariant convolutional networks. In *International conference on machine learning*, pp. 2990–2999. PMLR, 2016.
- Crassidis, J. L., Lai, K.-L., and Harman, R. R. Real-time attitude-independent three-axis magnetometer calibration. *Journal of Guidance, Control, and Dynamics*, 28(1):115–120, 2005.
- Davis, C. and Kahan, W. M. The rotation of eigenvectors by a perturbation. iii. *SIAM Journal on Numerical Analysis*, 7(1):1–46, 1970.
- Fuchs, F., Worrall, D., Fischer, V., and Welling, M. Se (3)-transformers: 3d roto-translation equivariant attention networks. *Advances in neural information processing systems*, 33:1970–1981, 2020.
- Gebre-Egziabher, D., Elkaim, G. H., David Powell, J., and Parkinson, B. W. Calibration of strapdown magnetometers in magnetic field domain. *Journal of Aerospace Engineering*, 19(2):87–102, 2006.
- Gnadt, A. R., Belarge, J., Canciani, A., Carl, G., Conger, L., Curro, J., Edelman, A., Morales, P., Nielsen, A. P., O’Keeffe, M. F., et al. Signal enhancement for magnetic navigation challenge problem. *arXiv preprint arXiv:2007.12158*, 2020.
- Gnadt, A. R., Belarge, J., Canciani, A., Carl, G., Conger, L., Curro, J., Edelman, A., Morales, P., Nielsen, A. P., O’Keeffe, M. F., Rackauckas, C. V., Taylor, J., and Wollaber, A. B. Signal enhancement for magnetic navigation challenge problem. *arXiv*, pp. 1–12, 2023a. doi: 10.48550/arXiv.2007.12158. URL <https://doi.org/10.48550/arXiv.2007.12158>.
- Gnadt, A. R., Belarge, J., Canciani, A., Conger, L., Curro, J., Edelman, A., Morales, P., O’Keeffe, M. F., Taylor, J., Jacobs, D., Rackauckas, C., Carl, G., and Wollaber, A. DAF-MIT AIA Open Flight Data for Magnetic Navigation Research, 2023b. URL <https://doi.org/10.5281/zenodo.4271803>.
- Hu, Y., Zhang, G., Liu, P., Lan, D., Li, N., Cheng, D., Dai, T., Xia, S.-T., and Pan, S. Timefilter: Patch-specific spatial-temporal graph filtration for time series forecasting. In *Forty-second International Conference on Machine Learning*, 2025. URL <https://openreview.net/forum?id=490VcNtjh7>.
- Huang, Z. and Van Gool, L. A riemannian network for spd matrix learning. In *Proceedings of the AAAI conference on artificial intelligence*, volume 31, 2017.
- Ionescu, C., Vantzos, O., and Sminchisescu, C. Matrix backpropagation for deep networks with structured layers. In *Proceedings of the IEEE international conference on computer vision*, pp. 2965–2973, 2015.
- Jolliffe, I. Principal component analysis. In *International encyclopedia of statistical science*, pp. 1094–1096. Springer, 2011.
- Kalman, R. E. A new approach to linear filtering and prediction problems. 1960.
- Lee, D.-Y., Yun, G., Choi, M., Cho, K.-H., Lee, J. D., and Lee, D.-H. Miniaturized dual-photodiode sensor for simultaneous wavelength and irradiance measurement across the 500–1000 nm range. *Applied Optics*, 63(35):9047–9053, 2024.
- Lee, H., Lee, H., Choi, M., Hwang, Y., and Lee, D.-Y. Portable single-beam atomic total-field magnetometer for stand-off magnetic sensing. *arXiv preprint arXiv:2601.08716*, 2026.
- Leliak, P. Identification and evaluation of magnetic-field sources of magnetic airborne detector equipped aircraft. *IRE Transactions on Aerospace and Navigational Electronics*, (3):95–105, 2009.
- Li, F., Fujiwara, K., Okura, F., and Matsushita, Y. A closer look at rotation-invariant deep point cloud analysis. In *Proceedings of the IEEE/CVF International Conference on Computer Vision*, pp. 16218–16227, 2021.

- Li, P., Xie, J., Wang, Q., and Gao, Z. Towards faster training of global covariance pooling networks by iterative matrix square root normalization. In *Proceedings of the IEEE conference on computer vision and pattern recognition*, pp. 947–955, 2018.
- Liu, Y., Hu, T., Zhang, H., Wu, H., Wang, S., Ma, L., and Long, M. itransformer: Inverted transformers are effective for time series forecasting. *arXiv preprint arXiv:2310.06625*, 2023.
- Nerrise, F., Sosanya, A. S., and Neary, P. Physics-informed calibration of aeromagnetic compensation in magnetic navigation systems using liquid time-constant networks. *arXiv preprint arXiv:2401.09631*, 2024.
- Nie, Y. A time series is worth 64words: Long-term forecasting with transformers. *arXiv preprint arXiv:2211.14730*, 2022.
- Satorras, V. G., Hoogeboom, E., and Welling, M. E (n) equivariant graph neural networks. In *International conference on machine learning*, pp. 9323–9332. PMLR, 2021.
- Tan, M., Merrill, M., Gupta, V., Althoff, T., and Hartvigsen, T. Are language models actually useful for time series forecasting? *Advances in Neural Information Processing Systems*, 37:60162–60191, 2024.
- Tancik, M., Srinivasan, P., Mildenhall, B., Fridovich-Keil, S., Raghavan, N., Singhal, U., Ramamoorthi, R., Barron, J., and Ng, R. Fourier features let networks learn high frequency functions in low dimensional domains. *Advances in neural information processing systems*, 33:7537–7547, 2020.
- Tolles, W. E. and Lawson, J. D. Magnetic compensation of mad equipped aircraft. *Airborne Instruments Lab. Inc., Mineola, NY, Rept*, pp. 201–1, 1950.
- Tuzel, O., Porikli, F., and Meer, P. Region covariance: A fast descriptor for detection and classification. In *European conference on computer vision*, pp. 589–600. Springer, 2006.
- Vaswani, A., Shazeer, N., Parmar, N., Uszkoreit, J., Jones, L., Gomez, A. N., Kaiser, Ł., and Polosukhin, I. Attention is all you need. *Advances in neural information processing systems*, 30, 2017.
- Wen, Q., Zhou, T., Zhang, C., Chen, W., Ma, Z., Yan, J., and Sun, L. Transformers in time series: A survey. *arXiv preprint arXiv:2202.07125*, 2022.
- Wu, H., Hu, T., Liu, Y., Zhou, H., Wang, J., and Long, M. Timesnet: Temporal 2d-variation modeling for general time series analysis. *arXiv preprint arXiv:2210.02186*, 2022.
- Yu, Y., Wang, T., and Samworth, R. J. A useful variant of the davis–kahan theorem for statisticians. *Biometrika*, 102(2):315–323, 2015.
- Zeng, A., Chen, M., Zhang, L., and Xu, Q. Are transformers effective for time series forecasting? In *Proceedings of the AAAI conference on artificial intelligence*, volume 37, pp. 11121–11128, 2023.
- Zhang, Y. and Yan, J. Crossformer: Transformer utilizing cross-dimension dependency for multivariate time series forecasting. In *The eleventh international conference on learning representations*, 2023.

A. Dataset Description

We use the public MagNav challenge dataset collected near Ottawa, Ontario, Canada, through a collaboration between the Department of the Air Force MIT AI Accelerator and Sanders Geophysics Ltd. The platform is a Cessna 208B Grand Caravan instrumented with multiple magnetometers and standard flight telemetry. The magnetic suite contains five scalar magnetometers that measure total field intensity and three vector magnetometers that measure tri axial field components. The scalar sensors are optically pumped units, and the vector sensors are fluxgate units. The sensors are installed at distinct locations across the airframe, which creates meaningful variation in interference strength and structure. One scalar sensor is mounted on a boom behind the cabin, which reduces coupling to onboard magnetic sources and serves as the reference signal for supervision. The remaining scalar sensors are placed inside the cabin at different longitudinal positions and heights, which makes them strongly affected by airframe fields and electrical activity.

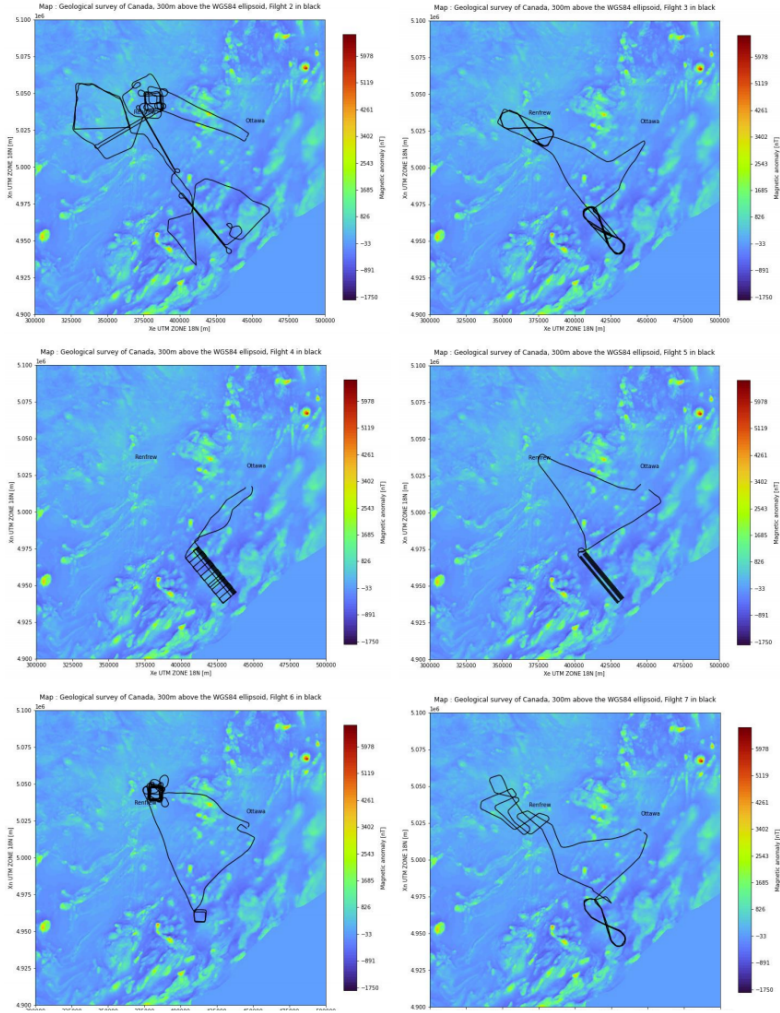


Figure 4. Flight path. Adapted from the MagNav repository (<https://github.com/Naatyu/MagNav>).

Table 6 summarizes the six flights, their segmentation, and their sample counts at 10 Hz. We partition the data to prevent spatial leakage where the aircraft revisits specific geographic locations. The training set comprises flights 1002 1004 and 1006 while flights 1003 and 1007 serve as unseen test cases. Flight 1003 features figure eight patterns and Flight 1007

Dataset	dim	Sequence Length	Prediction Length	Dataset Size
NV2	26	30, 60	60, 120	(124548, 41516, 41516)
NV3	26	30, 60	60, 120	(96018, 32006, 32006)
NV4	26	30, 60	60, 120	(48844, 16282, 16282)
NV6	26	30, 60	60, 120	(64990, 21664, 21664)
NV7	26	30, 60	60, 120	(68703, 22901, 22902)

Table 5. Summary of the MagNav flights used in our experiments

includes complex maneuvering which challenges the generalization capabilities of the models. We apply the International Geomagnetic Reference Field model to remove the core field component from the raw readings. Ground stations provide corrections for diurnal temporal variations which further isolates the local crustal magnetic field. The total recording time exceeds 20 hours with flight altitudes ranging between 400 meters and 800 meters. The geographic region exhibits low crustal field variation which simplifies the isolation of aircraft induced noise for benchmarking purposes. All flights occurred during the day to ensure consistent environmental conditions. See flight path visualization Figure 4.

B. Mathematical derivations

Proposition B.1 (Spectral Alignment of Canonical SPD). *Let $G = U\Lambda U^\top$ be the aggregated Gram matrix and $M(\mathbf{s}) = U\Sigma(\mathbf{s})U^\top$ the canonical SPD transform. Define the Gram matrix of the modulated triads as $\tilde{G}(\mathbf{s}) := \sum_{t=1}^L (\tilde{B}_t \tilde{B}_t^\top + \tilde{C}_t \tilde{C}_t^\top + \tilde{D}_t \tilde{D}_t^\top)$. Then $\tilde{G}(\mathbf{s}) = U\Sigma(\mathbf{s})\Lambda\Sigma(\mathbf{s})U^\top$. In particular, $\tilde{G}(\mathbf{s})$ has eigenvectors U and eigenvalues $\sigma_i(\mathbf{s})^2 \lambda_i$ for $i = 1, 2, 3$.*

Proof. Let $M := M(\mathbf{s})$. Since $\tilde{B}_t = MB_t$, we have

$$\tilde{B}_t \tilde{B}_t^\top = (MB_t)(MB_t)^\top = M(B_t B_t^\top)M^\top, \quad (25)$$

and similarly for \tilde{C}_t, \tilde{D}_t . Hence

$$\tilde{G}(\mathbf{s}) = \sum_{t=1}^L M(B_t B_t^\top + C_t C_t^\top + D_t D_t^\top)M^\top = MGM^\top. \quad (26)$$

Using $G = U\Lambda U^\top$ and $M = U\Sigma(\mathbf{s})U^\top$ with $U^\top U = I$ and Σ diagonal,

$$\tilde{G}(\mathbf{s}) = (U\Sigma U^\top)(U\Lambda U^\top)(U\Sigma U^\top) \quad (27)$$

$$= U\Sigma\Lambda\Sigma U^\top. \quad (28)$$

Therefore $U^\top \tilde{G}(\mathbf{s})U = \Sigma\Lambda\Sigma = \text{diag}(\sigma_1^2 \lambda_1, \sigma_2^2 \lambda_2, \sigma_3^2 \lambda_3)$, so u_i is an eigenvector of $\tilde{G}(\mathbf{s})$ with eigenvalue $\sigma_i^2 \lambda_i$. \square

C. Hyperparameter

We tuned hyperparameters via grid search to ensure a fair comparison across all baselines. The search space for general time series forecasting models covered a broad range of capacities. We varied the model dimension d_{model} within the set $\{64, 128, 256, 512\}$. We selected feed-forward dimensions d_{ff} from $\{64, 128, 256\}$. We tested encoder depths of 1, 2, 3, and 4 layers. The attention mechanism used either 2 or 4 heads. We adapted the search space for TimesNet to accommodate its specific structural requirements. We swept d_{model} values of $\{8, 16, 32, 64\}$ and d_{ff} values of $\{8, 16, 32\}$. We retained the same ranges for layers and heads. We additionally tuned the top- k parameter from $\{3, 5, 7\}$. We chose the final configuration for each model based on the lowest validation error. See the hyperparameter Table 6.

Panel A. General Time Series Forecasting Models	
Parameter	Values
D_MODELS	64, 128, 256, 512
D_FF	64, 128, 256
E_LAYERS_LIST	1, 2, 3, 4
N_HEADS_LIST	2, 4

Panel B. TimesNet	
Parameter	Values
D_MODELS	8, 16, 32, 64
D_FF	8, 16, 32
E_LAYERS_LIST	1, 2, 3, 4
N_HEADS_LIST	2, 4
TOP_K	3, 5, 7

Table 6. Hyperparameter grid search space

D. Complete results for IGRF forecasting

Panel A. Lookback window $L = 30$									
Methods	NavFormer	PatchTST	PAtn	TimeFilter	iTransformer	TimesNet	DLinear	LTC-CFC	
Metric	MAE	MAE	MAE	MAE	MAE	MAE	MAE	MAE	
NV2	60	0.0068 ± 0.0006	0.0062 ± 0.0000	0.0085 ± 0.0000	0.0082 ± 0.0007	0.0087 ± 0.0011	0.0116 ± 0.0009	0.0521 ± 0.0023	0.2780 ± 0.0190
	120	0.0352 ± 0.0001	0.0391 ± 0.0009	0.0366 ± 0.0004	0.0368 ± 0.0016	0.0387 ± 0.0007	0.0457 ± 0.0005	0.0954 ± 0.0010	0.2987 ± 0.0361
NV3	60	0.0094 ± 0.0005	0.0088 ± 0.0001	0.0107 ± 0.0001	0.0111 ± 0.0002	0.0118 ± 0.0001	0.0188 ± 0.0002	0.0713 ± 0.0040	0.2434 ± 0.0490
	120	0.0607 ± 0.0011	0.0609 ± 0.0004	0.0630 ± 0.0008	0.0695 ± 0.0010	0.0643 ± 0.0004	0.0784 ± 0.0020	0.1537 ± 0.0023	0.2208 ± 0.0192
NV4	60	0.0090 ± 0.0002	0.0095 ± 0.0003	0.0104 ± 0.0002	0.0107 ± 0.0005	0.0143 ± 0.0011	0.0248 ± 0.0015	0.0988 ± 0.0051	0.3485 ± 0.0667
	120	0.0386 ± 0.0005	0.0427 ± 0.0013	0.0604 ± 0.0005	0.0770 ± 0.0005	0.0889 ± 0.0010	0.0967 ± 0.0015	0.1609 ± 0.0040	0.3528 ± 0.0470
NV6	60	0.0339 ± 0.0012	0.0393 ± 0.0016	0.0390 ± 0.0007	0.0427 ± 0.0014	0.0487 ± 0.0010	0.0725 ± 0.0008	0.1941 ± 0.0051	0.3532 ± 0.0019
	120	0.2094 ± 0.0081	0.2279 ± 0.0162	0.2571 ± 0.0267	0.2548 ± 0.0077	0.2697 ± 0.0003	0.3102 ± 0.0137	0.4350 ± 0.0021	0.3650 ± 0.0053
NV7	60	0.0160 ± 0.0004	0.0158 ± 0.0003	0.0195 ± 0.0005	0.0221 ± 0.0002	0.0228 ± 0.0008	0.0278 ± 0.0014	0.0937 ± 0.0024	0.1281 ± 0.0027
	120	0.0880 ± 0.0022	0.0907 ± 0.0050	0.0954 ± 0.0066	0.0993 ± 0.0037	0.0907 ± 0.0004	0.1063 ± 0.0025	0.1538 ± 0.0006	0.3666 ± 0.0908

Panel B. Lookback window $L = 60$									
Methods	NavFormer	PatchTST	PAtn	TimeFilter	iTransformer	TimesNet	DLinear	LTC-CFC	
Metric	MAE	MAE	MAE	MAE	MAE	MAE	MAE	MAE	
NV2	60	0.0061 ± 0.0002	0.0085 ± 0.0003	0.0080 ± 0.0001	0.0089 ± 0.0001	0.0077 ± 0.0002	0.0123 ± 0.0006	0.0372 ± 0.0031	0.2770 ± 0.0209
	120	0.0369 ± 0.0001	0.0419 ± 0.0005	0.0377 ± 0.0001	0.0388 ± 0.0002	0.0389 ± 0.0001	0.0478 ± 0.0011	0.0843 ± 0.0023	0.2926 ± 0.0391
NV3	60	0.0127 ± 0.0005	0.0135 ± 0.0001	0.0127 ± 0.0001	0.0156 ± 0.0007	0.0154 ± 0.0001	0.0234 ± 0.0017	0.0551 ± 0.0033	0.2256 ± 0.0215
	120	0.0681 ± 0.0002	0.0681 ± 0.0009	0.0692 ± 0.0015	0.0729 ± 0.0010	0.0671 ± 0.0006	0.0809 ± 0.0006	0.1538 ± 0.0009	0.2206 ± 0.0191
NV4	60	0.0106 ± 0.0005	0.0120 ± 0.0004	0.0121 ± 0.0003	0.0115 ± 0.0004	0.0145 ± 0.0016	0.0234 ± 0.0016	0.0788 ± 0.0013	0.3416 ± 0.0554
	120	0.0397 ± 0.0012	0.0454 ± 0.0012	0.0533 ± 0.0044	0.0500 ± 0.0035	0.0779 ± 0.0007	0.0939 ± 0.0018	0.1499 ± 0.0012	0.3640 ± 0.0534
NV6	60	0.0394 ± 0.0021	0.0487 ± 0.0018	0.0462 ± 0.0014	0.0515 ± 0.0014	0.0572 ± 0.0017	0.0942 ± 0.0018	0.2289 ± 0.0048	0.3545 ± 0.0035
	120	0.2336 ± 0.0023	0.2246 ± 0.0068	0.2333 ± 0.0083	0.2385 ± 0.0102	0.2632 ± 0.0019	0.3129 ± 0.0055	0.4814 ± 0.0096	0.3636 ± 0.0043
NV7	60	0.0186 ± 0.0007	0.0202 ± 0.0002	0.0210 ± 0.0004	0.0238 ± 0.0012	0.0247 ± 0.0005	0.0408 ± 0.0008	0.0711 ± 0.0024	0.3497 ± 0.0058
	120	0.0971 ± 0.0011	0.0947 ± 0.0013	0.1056 ± 0.0020	0.0985 ± 0.0027	0.0974 ± 0.0009	0.1156 ± 0.0009	0.1383 ± 0.0006	0.3633 ± 0.0089

Table 7. Forecasting performance comparison. We report the Mean Absolute Error (MAE) averaged over prediction lengths $T \in \{60, 120\}$. **Panel A** presents results with a lookback window of $L = 30$, while **Panel B** uses a lookback window of $L = 60$. The best results are highlighted in red, the second-best in blue and third-best in bold, respectively.

Panel A. Lookback window $L = 30$									
Methods	NavFormer	PatchTST	PAtn	TimeFilter	iTransformer	TimesNet	DLinear	LTC-CFC	
Metric	RMSE	RMSE	RMSE	RMSE	RMSE	RMSE	RMSE	RMSE	
NV2	60	0.0235 ± 0.0006	0.0249 ± 0.0003	0.0253 ± 0.0002	0.0602 ± 0.0008	0.0283 ± 0.0016	0.0334 ± 0.0013	0.0837 ± 0.0060	0.3699 ± 0.0417
	120	0.0955 ± 0.0012	0.1015 ± 0.0003	0.1019 ± 0.0004	0.1011 ± 0.0002	0.1039 ± 0.0012	0.1160 ± 0.0012	0.1551 ± 0.0014	0.3839 ± 0.0429
NV3	60	0.0263 ± 0.0017	0.0252 ± 0.0001	0.0271 ± 0.0004	0.0365 ± 0.0010	0.0607 ± 0.0005	0.0409 ± 0.0001	0.1034 ± 0.0034	0.2995 ± 0.0465
	120	0.1342 ± 0.0025	0.1333 ± 0.0007	0.1362 ± 0.0024	0.1565 ± 0.0014	0.1344 ± 0.0003	0.1478 ± 0.0018	0.2241 ± 0.0034	0.2954 ± 0.0175
NV4	60	0.0474 ± 0.0002	0.0482 ± 0.0001	0.0498 ± 0.0002	0.0515 ± 0.0010	0.0498 ± 0.0011	0.0663 ± 0.0011	0.1368 ± 0.0041	0.4409 ± 0.0463
	120	0.1075 ± 0.0012	0.1115 ± 0.0020	0.1318 ± 0.0011	0.1637 ± 0.0024	0.1623 ± 0.0015	0.1764 ± 0.0019	0.2282 ± 0.0060	0.4448 ± 0.0375
NV6	60	0.0905 ± 0.0019	0.0970 ± 0.0029	0.1005 ± 0.0013	0.1117 ± 0.0012	0.1118 ± 0.0016	0.1466 ± 0.0027	0.2942 ± 0.0043	0.4343 ± 0.0024
	120	0.4461 ± 0.0160	0.4504 ± 0.0238	0.4895 ± 0.0264	0.4823 ± 0.0051	0.5004 ± 0.0011	0.5517 ± 0.0159	0.6801 ± 0.0024	0.4460 ± 0.0031
NV7	60	0.0361 ± 0.0009	0.0355 ± 0.0008	0.0424 ± 0.0011	0.0476 ± 0.0005	0.0470 ± 0.0014	0.0518 ± 0.0014	0.1281 ± 0.0027	0.3385 ± 0.0155
	120	0.1648 ± 0.0037	0.1725 ± 0.0033	0.1716 ± 0.0020	0.1887 ± 0.0058	0.1579 ± 0.0006	0.1752 ± 0.0019	0.2174 ± 0.0015	0.4444 ± 0.0925

Panel B. Lookback window $L = 60$									
Methods	NavFormer	PatchTST	PAtn	TimeFilter	iTransformer	TimesNet	DLinear	LTC-CFC	
Metric	RMSE	RMSE	RMSE	RMSE	RMSE	RMSE	RMSE	RMSE	
NV2	60	0.0241 ± 0.0006	0.0280 ± 0.0011	0.0269 ± 0.0003	0.0321 ± 0.0007	0.0297 ± 0.0002	0.0373 ± 0.0009	0.0604 ± 0.0038	0.3674 ± 0.0439
	120	0.1032 ± 0.0001	0.1037 ± 0.0002	0.1024 ± 0.0003	0.1044 ± 0.0004	0.1065 ± 0.0003	0.1173 ± 0.0019	0.1446 ± 0.0014	0.3893 ± 0.0581
NV3	60	0.0326 ± 0.0008	0.0604 ± 0.0002	0.0323 ± 0.0002	0.0404 ± 0.0014	0.0371 ± 0.0004	0.0511 ± 0.0033	0.0803 ± 0.0031	0.2861 ± 0.0361
	120	0.1506 ± 0.0005	0.1435 ± 0.0013	0.1508 ± 0.0051	0.1587 ± 0.0031	0.1416 ± 0.0007	0.1531 ± 0.0010	0.2285 ± 0.0014	0.2950 ± 0.0174
NV4	60	0.0550 ± 0.0016	0.0492 ± 0.0006	0.0509 ± 0.0002	0.0524 ± 0.0003	0.0515 ± 0.0014	0.0687 ± 0.0055	0.1135 ± 0.0003	0.4321 ± 0.0443
	120	0.1122 ± 0.0024	0.1117 ± 0.0016	0.1253 ± 0.0055	0.1257 ± 0.0047	0.1515 ± 0.0015	0.1764 ± 0.0020	0.2201 ± 0.0015	0.4571 ± 0.0421
NV6	60	0.0988 ± 0.0036	0.1112 ± 0.0021	0.1126 ± 0.0027	0.1232 ± 0.0024	0.1268 ± 0.0024	0.1901 ± 0.0010	0.3477 ± 0.0050	0.4355 ± 0.0035
	120	0.4790 ± 0.0029	0.4502 ± 0.0055	0.4770 ± 0.0134	0.4690 ± 0.0077	0.4992 ± 0.0027	0.5604 ± 0.0050	0.7332 ± 0.0095	0.4411 ± 0.0025
NV7	60	0.0421 ± 0.0011	0.0407 ± 0.0005	0.0452 ± 0.0009	0.0499 ± 0.0022	0.0489 ± 0.0006	0.0738 ± 0.0015	0.1027 ± 0.0016	0.4216 ± 0.0044
	120	0.1802 ± 0.0010	0.1836 ± 0.0021	0.1928 ± 0.0035	0.1833 ± 0.0046	0.1707 ± 0.0004	0.1928 ± 0.0034	0.2047 ± 0.0005	0.4429 ± 0.0033

Table 8. Forecasting performance comparison. We report the Root Mean Squared Error (RMSE) averaged over prediction lengths $T \in \{60, 120\}$. **Panel A** presents results with a lookback window of $L = 30$, while **Panel B** uses a lookback window of $L = 60$. The best results are highlighted in red, the second-best in blue and third-best in bold, respectively.